

Comprehensive Analysis of Float Current Behavior and Calendar Aging Mechanisms in Lithium-Ion Batteries

Mohamed Azzam,* Dirk-Uwe Sauer, Christian Endisch, and Meinert Lewerenz

Aiming to quantify degradation currents from solid electrolyte interphase formation ($I_{SEIgrowth}$) and gain of active lithium due to cathode lithiation (I_{CL}), resulting from electrolyte decomposition, the float current behavior of lithium-ion batteries is investigated with different cathode materials. The float current, I_{float} , represents the recharge current required to maintain the cell at a fixed potential during calendar aging. This current arises as lithium is irreversibly consumed at the anode or inserted into the cathode, shifting the electrode potentials. To account for the asymmetric response of the electrodes, a voltage-dependent scaling factor, SF, is introduced, derived from the slopes of

the electrode-specific voltage curves. Using this factor in combination with measured float currents and capacity loss rates from check-up tests, $I_{SEIgrowth}$ and I_{CL} is quantified at 30 °C across various float voltages. Although the SF and capacity data are limited to 30 °C, the model is extended to a range of 5–50 °C using only float current measurements. The results show that using capacity loss rates alone underestimate $I_{SEIgrowth}$ and that I_{CL} contributes significantly to the observed float current at elevated voltages, indicating that cathode lithiation plays an increasingly important role in high-voltage calendar aging.

1. Introduction

The rise of electric vehicles (EVs) and renewable energy systems has positioned lithium-ion batteries as a cornerstone of modern energy technology. These batteries are highly valued for their superior energy and power density, making them the preferred choice for EVs.^[1] However, the long-term performance and lifespan of lithium-ion cells are constrained by aging processes, which are predominantly driven by the growth of the solid

electrolyte interphase (SEI), lithium plating, and the loss of active material(LAM).^[1] Aging in lithium-ion batteries is typically classified into two categories: operational (cyclic aging) and storage-related (calendar aging). For applications requiring longevity, such as EVs, calendar aging plays a critical role, as it primarily occurs during periods of storage.^[2] This type of aging is most strongly influenced by storage temperature and state of charge (SoC).

Under moderate conditions, calendar aging is primarily characterized by a loss of lithium inventory (LLI) and increased internal resistance due to SEI growth as reported in.^[3–5] These effects are commonly evaluated using periodic check-up tests that include capacity and pulse tests.^[6,7] While capacity measurements are widely used to assess aging, they are subject to several limitations. Frequent testing can shift the aging mode toward cyclic aging,^[8,9] and reversible effects—such as anode overhang and polarization—can dominate early-stage results, obscuring actual degradation.^[10–15] Moreover, the accuracy of capacity tests is compromised under low aging rates or variable thermal conditions. Standard protocols typically require constant temperatures above 20 °C,^[16–19] which do not reflect real-world conditions. Reversible and dynamic influences, especially at low temperatures, further reduce the reliability of capacity-based diagnostics, as shown by de Hoog et al.,^[20] Rumberg et al.,^[21] and Bouchhima et al.^[22]

An emerging complementary measurement technique for evaluating even minimal self-discharge rates is the float current analysis. This technique involves monitoring the trickle charge during extended potentiostatic holds and associating it with calendar aging. Recent studies have shown a strong correlation between float current and capacity loss rates, as demonstrated by Lewerenz et al.^[23] and Theiler et al.^[24] In our previous research,^[20] we identified a crucial link between float currents

M. Azzam, C. Endisch, M. Lewerenz
Research Group Electromobility and Learning Systems
Technische Hochschule Ingolstadt
D-85049 Ingolstadt, Germany
E-mail: mohamed.azzam@thi.de

M. Azzam, D.-U. Sauer
Chair for Electrochemical Energy Conversion and Storage Systems
Institute for Power Electronics and Electrical Drives (ISEA)
RWTH Aachen University
Campus-Boulevard 89, 52074 Aachen, Germany

D.-U. Sauer
Jülich Aachen Research Alliance
JARA-Energy
Templergraben 55, 52056 Aachen, Germany

D.-U. Sauer
Institute for Power Generation and Storage Systems (PGS)
E.ON ERC
RWTH Aachen University
Mathieustrasse 10, 52074 Aachen, Germany

D.-U. Sauer
Helmholtz Institute Münster (HI MS), IEK 12
Forschungszentrum Jülich
52425 Jülich, Germany

© 2025 The Author(s). *Batteries & Supercaps* published by Wiley-VCH GmbH.
This is an open access article under the terms of the Creative Commons Attribution License, which permits use, distribution and reproduction in any medium, provided the original work is properly cited.

and the development of the SEI layer, particularly at lower SoCs, while also observing significant cathode-related effects at higher SoCs.^[25] This separation was possible with the help of the scaling factor **SF**, which is the ratio of the respective half-cell open-circuit voltage (OCV) to the full cell OCV. For each electrode, the scaling factor determines, how much of the aging-induced current corresponding to the measured float current is recharged on each electrode. It indicates that at higher SoCs the measured float current must be associated with the cathode as the voltage curve of the anode is comparably flat and will not cause any recharge current. Other researchers, including Streck et al.^[26] have proposed that phenomena observed at higher voltages may be due to coupled-side reaction such as a shuttle reactions causing no aging but reducing the SoC. However, while distinguishing shuttle reactions from cathode lithiation (CL) typically requires postmortem analysis, shuttle reactions are unlikely to cause the notable increase in internal resistance observed typically at higher voltages.^[27,28]

CL, as described by Keil et al.^[29] occurs when lithium ions from electrolyte decomposition become incorporated actively into the cathode material, leading to increased internal resistance and gain of capacity over time. This theory was reinforced by Hartmann et al.^[30] who demonstrated that at high voltages and temperatures, the conductive salt (LiPF_6) decomposes, introducing additional active lithium into the cathode but increases internal resistance, which affects the performance during cycling significantly. Therefore, CL is, besides SEI growth, a pivotal aging mechanism.

Additionally, Boetticher et al.^[31] highlighted the use of PTFE (polytetrafluoroethylene) tape to tighten the jelly roll in pouch cells causes a self-discharge due to a shuttle reaction. However, PTFE is not typically employed in cylindrical cells, and they further noted that this effect is strongly suppressed in the presence of vinylene carbonate (VC). As in the investigated cells for float currents no PTFE tape was found, it is suggested that CL is the more probable cause of the increased resistance and capacity loss seen at higher voltages, rather than shuttle reactions.

To understand the potential different impact of OCV and constant voltage tests, Azzam et al.^[32] explored the relationship between OCV and float current measurements across various voltages and temperatures, focusing on entropy effects^[33] and the resulting steady-state currents after extended voltage holds. Their findings confirmed that float current measurements consistently track the same aging processes without triggering additional degradation mechanisms during trickle charge compared to OCV tests.

Despite significant advancements in understanding the correlation between float current measurements and battery aging, certain aspects remain underexplored. While the relationship between SEI growth and float currents has been well documented, the effects of CL under varying operational conditions have not been fully investigated. However, systematic studies quantifying these aging processes across various cell chemistries, voltages, and temperatures are still limited.

In our previous work,^[20] we introduced a model that linked SEI formation losses to the capacity loss rate using the scaling factor.

It showed that additional mechanisms, such as CL, might explain observed discrepancies between modeled and measured float currents at higher SoCs at 30 °C only.

In this work, we present a novel float current-based aging model that enables mechanism-specific quantification of SEI growth and CL currents. The approach combines steady-state float current measurements, capacity loss rates, and electrode-specific scaling factors to resolve degradation contributions at the anode and cathode independently. We validate this framework on two commercial lithium-ion cells with different cathode chemistries by linking float current behavior to capacity fade across a broad range of applied float voltages and temperatures. In Section 2.2, we describe the methodology for float current measurements and the derivation of voltage-dependent scaling factors, which are used to separate electrode-specific contributions. Section 2.3 introduces a model framework that enables the decomposition of float current into SEI growth and CL currents. This framework is then applied in the results section, where we first analyze capacity loss and resistance trends from periodic check-ups, followed by the evaluation of float current behavior across voltage and temperature ranges. The model is subsequently used to quantify electrode-specific degradation currents, and extended to account for temperature effects.

2. Experimental Section

2.1. Experimental, Equipment and Test Setup

For this study, 17 cylindrical 18 650 cells of two different types were investigated, each featuring a pure graphite anode but differing in cathode active materials and nominal capacities. Detailed information about these test cells, referred to as A123 and PAN, is provided in **Table 1**. The cells were tested using a custom-developed device specifically designed for float current measurements, referred to as the "Floater." The Floater (Version 2.0) is capable of high-precision voltage measurements with an accuracy of $\pm 0.4 \mu\text{V}_{\text{rms}}$ and current measurements down to $\pm 1.0 \text{nA rms}$. This system ensures reliable performance for float current analysis, surpassing standard cyclers. Each unit integrates

Table 1. Specifications of the three used battery cell types.

Short Name	A123	PAN
Producer	A123	Panasonic
Cell type	APR18650M-A1	NCR18650B
Cathode	LFP	NCA
Anode	Graphite	Graphite
Nom. Capacity	1.1 Ah	3.2 Ah
Cell voltage range	2.0–3.6 V	2.5–4.2 V
Examined float voltages	3.2 V, 3.33 V, 3.34 V, 3.35 V, 3.36 V, 3.38 V, 3.4 V, 3.5 V, 3.6 V	3.368 V, 3.432 V, 3.62 V, 3.75 V, 3.821 V, 3.9 V, 4.0 V, 4.2 V

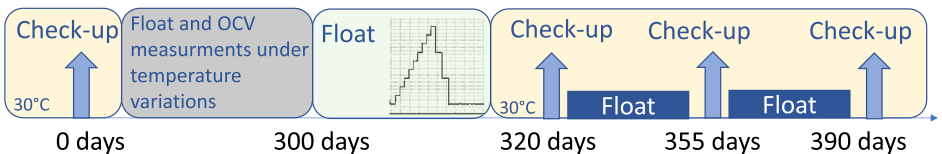


Figure 1. Measurement procedure for the cells.

universal temperature and humidity sensors, ensuring consistent measurement conditions across all channels. Detailed specifications of this measurement device are available in the referenced work by Azzam et al.^[32] The cells are housed and tested in a Binder temperature chamber (model KB115 (E4)), with the floater device placed in a separate Binder temperature chamber to ensure consistent thermal conditions at 25 °C. Additionally, the check-up tests as well as the galvanostatic intermittent titration technique (GITT) measurements were conducted using a 0–5 V/5 A LBTA2030 battery-cycler from Arbin Instruments.

The examined float voltages were selected based on the characteristic features of the half-cell DVA curves, ensuring coverage across voltage regions with distinct lithium exchange activity. These regions later correspond to strong contributions in the scaling factor, which was derived from the electrode-specific voltage slopes. The test procedure outlined in Figure 1 aims to correlate the capacity loss rates from the check-up procedure with the measured float current to quantify contributions of the anode and cathode.

Before the test execution, all cells were not fresh but underwent OCV and float measurements for a previous study, indicated in gray, which were not within the scope of this paper. While these measurements were not strictly necessary to stabilize the cells, they helped minimize reversible aging effects such as polarization and anode overhang.^[10] For the float current analysis, the history of aging was not important as only the present aging rate was measured. As a result, starting from day 300, no other reversible aging effects were evident. The float current evaluated in this study corresponds to the steady-state float current only, representing the cell's aging process.

The test procedure begins with an initial check-up at 30 °C, following a method similar to that presented by Theiler et al.^[24] During this check-up, the pulse test at 100% SoC and the capacity test at a low C-rate, which also supports differential voltage analysis (DVA), were evaluated. After the initial check-up and the previous study (gray), the cells were subjected to a float process while following a step profile that gradually increases the temperature in 5 K increments, ranging from 5 to 50 °C as indicated in green. Between each temperature step, a 24 h hold period was implemented to allow the entropy effects to subside, ensuring that the measured float current reflects only aging-related changes. The mean value over the final 6 h of each hold period is calculated before moving to the next temperature step. The only exception was the A123 cell at 3.6 V, which did only undergo the float and check-up tests but missed the temperature step test, unintentionally.

Finally, three additional check-ups were conducted at 30 °C for the 14 cells, spaced 35 days apart to determine the capacity loss

rate. Between these check-ups, the cells were maintained at their respective float voltages at 30 °C. All cells, with the exception of the A123 cells at 3.4, 3.5, and 3.6 V, followed the aforementioned three additional check-ups procedure. These three cells were added later to expand the voltage range and underwent additional check-ups at the beginning of the tests and instead of the three check-ups conducted at the end of the test period for the other cells, these three A123 cells had only one final check-up, resulting in a slightly shorter overall test duration.

2.2. Influence of Aging on Electrode Scaling Factors and Recharge Current Distribution

Based on the developed theory by Schulze et al.^[25] and validated by Azzam et al.^[34] the float procedure can be divided into a two-step process based on the voltage slippery theory. As a precondition, the cell was assumed to be perfectly held at a fixed full cell float voltage without any redistribution current within the electrodes before.

For the first step, we turn the constant voltage into OCV mode for a very short time. Due to calendar aging, a change in lithiation degrees on the respective electrode was triggered causing a voltage decay of the full cell. This change in lithiation degree can be described by continuous electrode-specific loss currents that are integrated for the specific time frame.

The primary aging process, the SEI, attributes to a passivation on the anode leading to a lower lithiation and with this to a higher anode potential and a lower full cell potential. The second part involves the recharge current required to restore the full cell float voltage. This recharge current depends on the slopes of both, the anode and cathode OCV curves compared to the slope of the full cell voltage curve at the given float voltage. Together they define the scaling factor, SF. As the aging-induced voltage decay on the anode leads during the recharge to a voltage rise on the cathode, the anode aging has as well an impact on the cathode potential.

The anode scaling factor SF_A that links the recharge current I_{Recharge} with the SEI growth rate $I_{\text{SEIgrowth}}$ is determined by evaluating the slopes of the anode and cathode half-cells and is calculated as

$$SF_A = \frac{I_{\text{Recharge}}}{I_{\text{SEIgrowth}}} = \frac{|k_{\text{Anode}}|}{|k_{\text{Fullcell}}|} = \frac{|k_{\text{Anode}}|}{|k_{\text{Anode}}| + |k_{\text{Cathode}}|} = \frac{1}{1 + \frac{|k_{\text{Cathode}}|}{|k_{\text{Anode}}|}} \quad (1)$$

As noted by Azzam et al.^[34] this relationship is explaining the measured float current quite well only for lower float voltages. Towards higher voltages, another effect becomes evident. This

effect, known as CL, as described and postulated by Keil et al.^[29] and Hartmann et al.^[30] behaves similarly to SEI but causes the cathode curve to shift toward lower cathode voltage by incorporating active lithium from conductive salt decomposition reducing the overall full cell voltage as well. Analogous to the SEI, the CL leads during the recharge to voltage decay of the anode.

The cathode scaling factor SF_c between the recharge current, influenced by the voltage slippery, and the CL growth rate I_{CL} is

$$SF_c = 1 - SF_A = \frac{I_{Recharge}}{I_{CL}} = \frac{|k_{Cathode}|}{|k_{Fullcell}|} = \frac{|k_{Cathode}|}{|k_{Anode}| + |k_{Cathode}|} \quad (2)$$

$$= \frac{1}{1 + \frac{|k_{Anode}|}{|k_{Cathode}|}}$$

If only SEI formation is present, the relationship is described by Equation (1), where the recharge current is solely attributed to $I_{SEIgrowth}$. Similarly, if CL occurs without SEI formation, (Equation 2) applies, with the recharge current associated only with I_{CL} .

To accurately model the SEI growth and CL effects from float currents, we must determine the appropriate scaling factor curves for both electrodes. This was achieved by following the methodology described by Azzam et al.^[34] which involves measuring the GITT in charge and discharge directions for each cell type. The resulting data was then averaged to obtain the pseudo-OCV curve. The differentiation of the pseudo-OCV provides the necessary insights to distinguish the characteristics of both electrodes. An educated-guess approach was applied to separate the full cell DVA in shares of each individual electrode based on characteristic shapes of the half-cell DVAs. Besides the characteristic shape of the half-cells, this procedure takes into account contributions of size, specific format, and pressure distribution of the housing, including anode overhang effect leading to less sharp peaks of the graphite anode. This results in a static scaling factor corresponding to the present usable capacity. It does not account for the aging-induced loss of active lithium, which shifts anode versus cathode according to the voltage slippery theory.

To consider the effect of aging based on the voltage slippery theory on the scaling factor, we visualized a graphite anode and a nickel-based cathode using a three-electrode cell setup, scaled to match the capacity of the PAN cell, as depicted in Figure 2a.

In our simulation, we aligned the anode and cathode potential changes over time with their corresponding OCV curves assuming loss of active lithium as a calendar aging mechanism. Since the lithiation degrees of the anode and cathode do not match over aging, we shift the cathode curve to the left based on the voltage slippery theory, while keeping the graphite anode position fixed. With this, the charge of the anode was set equal to the full cell's charge. The resulting curves generate new full cell OCV curves, as shown in Figure 2b. The shift in the OCV curve aligns with the expected aging behavior, serving as a validation.^[35,36] While the maximum cut-off voltage remains consistent, the lithiation degree of the full cell continually decreases, leading to lower capacities over time. From the half-cell voltage curves, we calculate anode scaling factor SF_A as shown in Figure 2c. The characteristic shape of the scaling factor remains unchanged but shifts to higher float voltages. For a fixed float voltage, the position of on the scaling factor curves changes and moves to characteristics originally present at lower float voltages.

2.3. Calendar Aging Model Framework

To analyze degradation mechanisms from the measured float currents I_{Float} , we postulate and apply a model that separates the electrode-specific contributions to the total measured recharge current. The framework integrates three directly measured parameters for each float voltage at 30 °C: 1) the capacity loss rate derived from check-up tests $I_{C_{loss}}$ (after the decay of the reversible effects, especially anode overhang), 2) the steady-state float current I_{Float} (after eliminating reversible effects such as anode overhang), and 3) electrode scaling factors SF extracted from GITT-based pseudo-OCV profiles. Based on these inputs, the net degradation rate observed from check-up capacity loss $I_{C_{loss}}$ is expressed in the capacity domain as,

$$I_{C_{loss}} = I_{SEIgrowth} - I_{CL} \quad (3)$$

Notably, the CL current I_{CL} reduces the observed capacity loss and may mask higher SEI-related aging $I_{SEIgrowth}$, if capacity data is used alone. Although both SEI growth and CL alter the full cell's lithium inventory, they were not in direct competition for Li⁺. SEI growth involves lithium-consuming reduction reactions at the

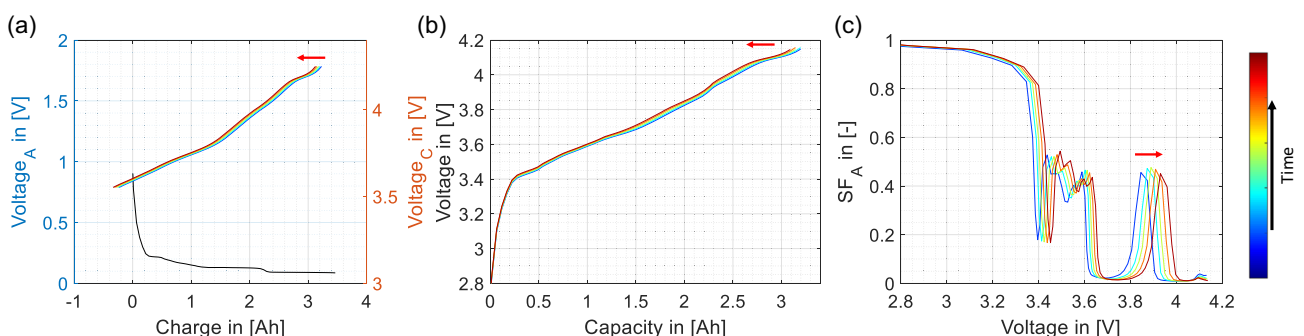


Figure 2. a) Anode half-cell OCV curve in black and cathode half-cell OCV curve over aging time. b) The resulting full cell OCV curve over time. c) The resulting anode scaling factor (SF_A) over time. The color scheme represents the effect of the aging time.

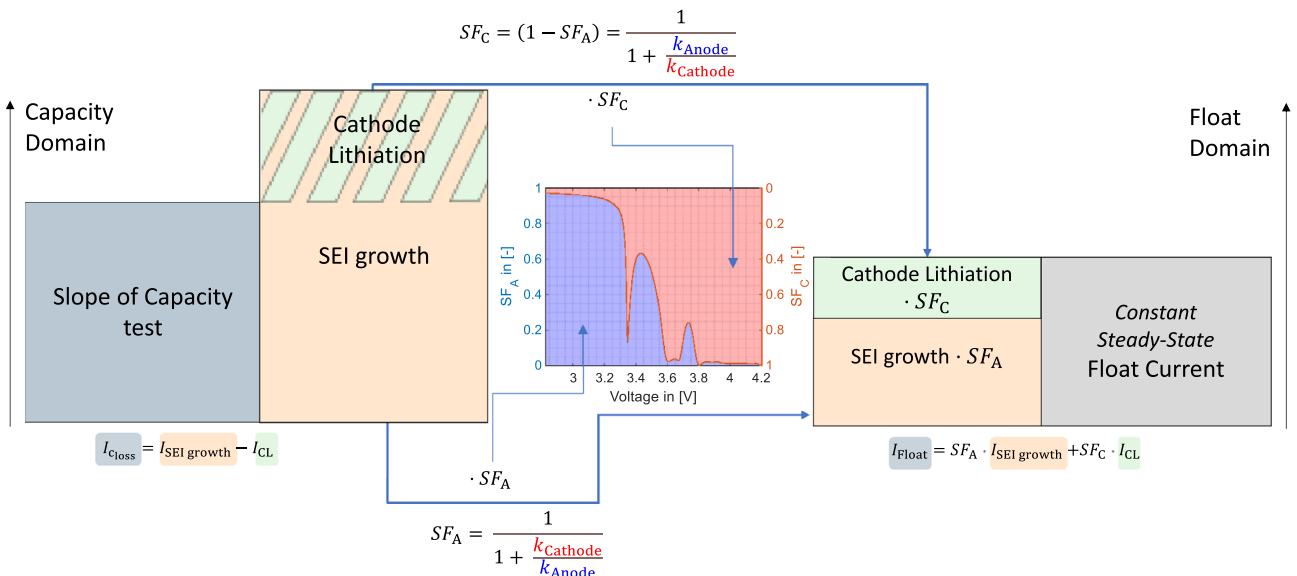


Figure 3. Model development for the determination of $I_{\text{SEI growth}}$ and I_{CL} based on the float and check-up procedure, and the scaling factor.

anode, while CL was associated with excess lithium resulting from oxidative electrolyte decomposition. These processes occur at different electrodes and were governed by distinct mechanisms. We therefore treat them as independent within the model—a simplification that aligns with observed behavior under float conditions. However, the relative contribution of each mechanism may vary depending on cell chemistry and design, and this balance could differ in other cell formats or under different storage conditions.

The model describes the measured float current I_{float} . It reflects the total recharge current I_{recharge} required to maintain the full cell voltage, which under real conditions results from both SEI formation at the anode and CL at the cathode, each weighted by their respective scaling factors SF_A and SF_C .

$$I_{\text{float}} = I_{\text{recharge}} = SF_A \cdot I_{\text{SEI growth}} + SF_C \cdot I_{\text{CL}} \quad (4)$$

For consistency, all currents are defined as positive, as both SEI formation and CL contribute to a loss of full cell voltage. It is important to note that, in our analysis, we assume the shuttle reaction by an internal self-discharge reaction without triggering aging as reported by Streck et al.^[26] to be negligible. This assumption is further supported by recent findings from Yu et al.^[37] who performed calendar aging studies using three-electrode cells and demonstrated, through both float current and OCV analysis, that SEI growth and CL fully account for observed capacity fade. Their results showed excellent agreement with capacity check-up tests and impedance trends, validating that shuttle reactions can be excluded without loss of accuracy. Additional support comes from ICP-OES and EIS measurements conducted in a follow-up study, which showed lithium and phosphorus redistribution consistent with SEI growth and cathode-side electrolyte decomposition. Therefore, we exclude shuttle mechanisms from our calculations

and instead focus on SEI growth and CL as the primary degradation processes.

According to (Equation 4) and the fact that SF is a value between 0 and 1, $I_{\text{SEI growth}}$ and I_{CL} induced currents are in the float domain equal or smaller compared to the capacity domain.

The model diagram summarizing this evaluation approach is shown in Figure 3.

Solving this system enables the extraction of the individual degradation currents $I_{\text{SEI growth}}$ and I_{CL} .

3. Results and Discussion

In the following, we aim to establish a quantitative relationship between float current measurements and conventional capacity loss. First, we evaluate the results from the check-up procedure, including the determination of the capacity loss rate I_{loss} , resistance trends and DVA (Section 3.1). Then, we investigate the behavior of the measured float current I_{float} under varying float voltages and temperatures (Section 3.2) and compare these trends to the voltage-dependent scaling factors SF derived from GITT measurements.

Next, we apply the model introduced in Section 2.3 to decompose the float current I_{float} into electrode-specific degradation currents: the anode-side contribution $I_{\text{SEI growth}}$, associated with SEI growth, and the cathode-side contribution I_{CL} , associated with CL (Section 3.3). This decomposition enables direct quantification of the individual degradation processes active at 30 °C for each float voltage. Finally, we extend the model to account for the temperature dependence of these degradation pathways. This allows us to quantify how both $I_{\text{SEI growth}}$ and I_{CL} evolve with temperature and to assess their relative contributions under different thermal conditions (Section 3.4).

3.1. Check-up Analysis: Capacity Loss Rate, Pulse Resistance and DVA

In the first step, we closely examine the 0.1 C charge and the pulse test at 100% SoC for the PAN cell, as illustrated in Figure 4a,b. From the 0.1 C charge data, the capacity loss rate $I_{C_{loss}}$ is derived.

As analyzed by Azzam et al.^[34] reversible effects such as polarization and anode overhang^[10] influence the measured capacity loss rate and the pulse test results. These effects persist for up to 90 days, after which a linear trend becomes apparent. Therefore, to calculate the capacity loss rate, represented by the slope indicated exemplary by the blue triangle for the 3.432 V cell, we focus on the three check-ups conducted starting at 320 days. The capacity loss rate appears almost linear, as expected, suggesting that all transient effects influencing capacity loss have diminished. This allows for a simplified quantification of the irreversible aging mechanisms. A slight increase in capacity is observed between the first and second check-up for the PAN cells at 3.62 and 4.2 V. These deviations appear to be transient and are treated as early effects that are not representative of the

long-term degradation trend. At 4.2 V, the float voltage slightly exceeds the standard formation cutoff voltage, likely inducing additional cathode delithiation and resulting in a one-time capacity boost.^[38] At 3.62 V, no definitive mechanistic explanation is available. In both cases, the subsequent check-ups exhibit the expected monotonic capacity fade. Therefore, the initial capacity increase has no impact on our evaluation, as the model focuses exclusively on the steady-state aging rate observed during the float period, after the decay of transient effects.

From the second to the fourth check-up, which are most relevant for quantifying the aging mechanisms, the cell at 4.2 V shows the highest capacity loss rate. In the pulse tests, the highest resistance is observed at the three highest voltage points, with an increase of up to 57%, while, besides a similar linear increase, no systematic trends according to voltage and initial value appear at lower voltages of 3.821 V and lower.

For the A123 cell, the capacity loss rates and pulse test results are shown in Figure 5a,b.

Due to limited test channel availability, the A123 cell at 3.35 V underwent the last three check-up procedures after the completion of all other cells. In the beginning, the influence of the anode

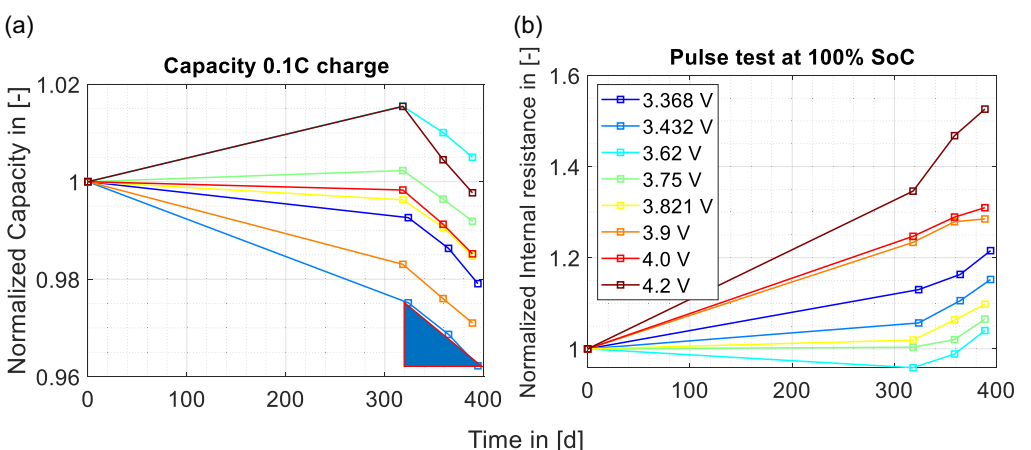


Figure 4. a) Normalized capacity from the 0.1 C charge procedure and b) pulse resistance at 100% SoC trends measured in check-ups for the PAN cell.

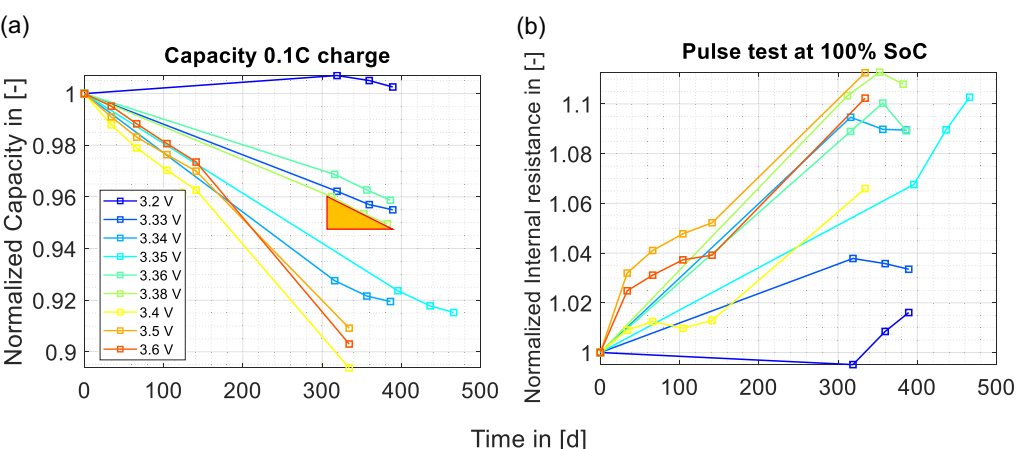


Figure 5. a) Normalized capacity from the 0.1 C charge procedure and b) pulse resistance at 100% SoC trends measured in check-ups for the A123 cell.

overhang effect is observable. At 3.2 V, an increase exceeding 100% is measured, consistent with lithium redistribution from previously inactive anode regions.^[10] This is expected, as the lowest voltage draws lithium from the anode overhang and can therefore increase above the initial capacity. For the cells at 3.4, 3.5, and 3.6 V, we conducted additional check-ups as mentioned in Section 2.1. In this case, capacity degradation did not follow a single linear trend but exhibited two distinct linear regions. The reason for this deviation from typical behavior is unclear. However, since the float temperature tests were conducted during the second linear phase, we used that segment to calculate the degradation current, ensuring alignment with the relevant test conditions. Counterintuitively, the capacity loss rate of the 3.38 V cell is lower than that of 3.33 and 3.34 V.

For all A123 cells, there is no clear correlation between resistance and voltage; however, an overall increase is observed, with a maximum rise of 13% at 3.6 V (see Figure 5b). The 3.38 V cell, despite having a relatively low capacity loss rate, exhibits one of the highest internal resistances. This suggests the presence of an underlying effect, such as electrolyte decomposition leading to CL, which could be masking the actual capacity loss.

To further investigate the underlying degradation mechanisms, we analyze the DVAs of both cells across all voltages. DVA provides insights into aging effects, particularly LLI and the LAM on the anode or cathode.^[12,39] In the context of calendar aging, literature consistently points to LLI as the primary factor influencing battery capacity, especially under mild aging conditions.^[40] Consequently, the capacity decay observed during check-ups is typically attributed to LLI.

In the DVA curves of the PAN cell, shown in Figure 6, the two lower-voltage peaks are attributed to the anode ($P_{A,1}$ and $P_{A,2}$), while the higher-voltage peaks are assigned to the cathode

($P_{C,1}$ and $P_{C,2}$). With aging, the anode-associated peaks progressively shift to lower capacities, especially at float voltages of 3.821, 4.0, and 4.2 V. In contrast, the cathode peaks remain stable in both shape and position.

This indicates that there is no significant LAM on either electrode. Since the cathode peaks are unchanged, cathode degradation can be excluded. The shift of the anode peaks suggests that lithium is being removed from the system (LLI).

In the DVA curves of the A123 cell, seen in Figure 7, the low-voltage peaks $P_{A,1}$ and $P_{A,2}$ are attributed to the anode, while the high-voltage region near full capacity corresponds to the LFP cathode P_C . Over the aging period, the anode peaks shift gradually to lower capacities, particularly at float voltages of 3.4 V and above. This shift indicates lithium loss.

The overall shape of the anode peaks remains stable, suggesting no significant LAM on the anode. For the LFP cathode, no distinct peaks are visible apart from the saturation region near 100% SoC, which is characteristic for this chemistry. Consequently, LAM on the cathode side cannot be evaluated from DVA, and based on literature,^[41] LFP degradation at 30 °C is assumed to be negligible.

Since no evidence of LAM is observed and the only clear signature is the shift of the anode peaks, the DVA results support the interpretation that aging is dominated by LLI, likely driven by SEI growth on the anode. The possible influence of CL, which would act as a gain mechanism and reduce apparent capacity loss, is not captured in DVA. Overall, the DVA confirms that the dominant aging process in the A123 cell is LLI, with no signs of structural electrode degradation under the tested conditions.

In summary, the DVA analysis confirms that LLI is the main contributor to calendar aging for both cell types under the tested conditions. However, DVA alone does not allow separation of

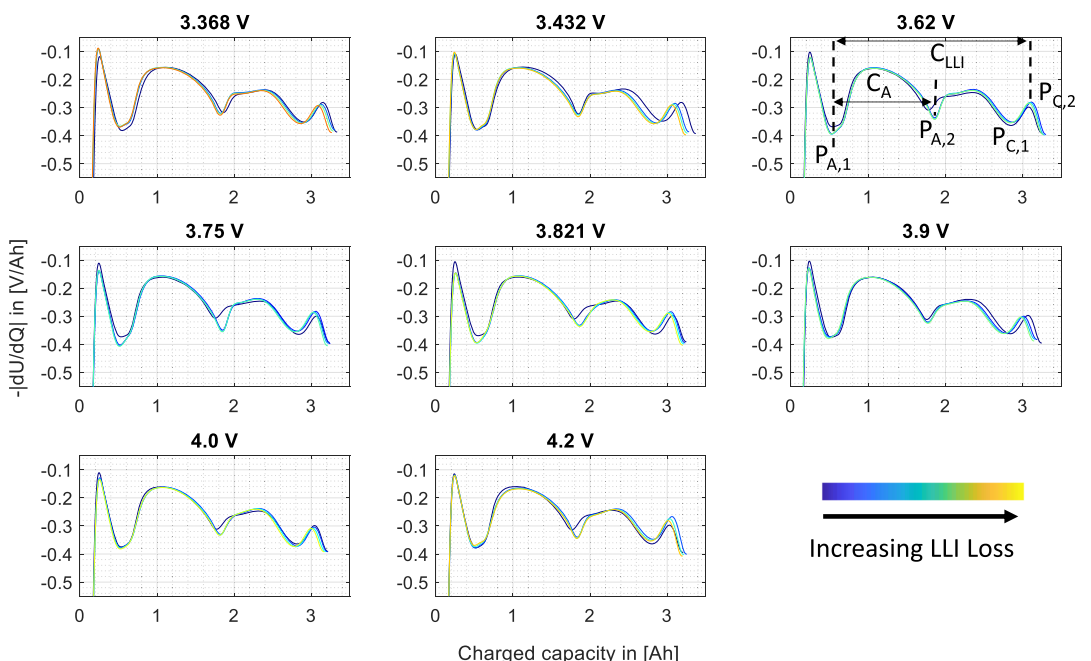


Figure 6. DVA measurements over check-ups at different float voltages during charging for the PAN cell.

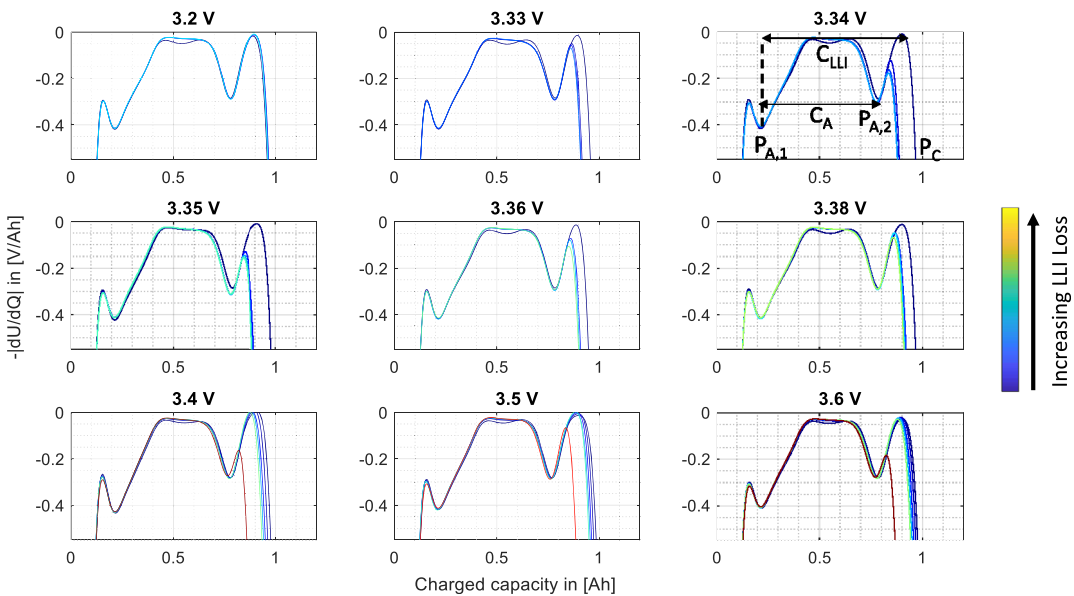


Figure 7. DVA measurements over check-ups at different float voltages during charging for the A123 cell.

individual electrode-side processes, such as SEI growth and CL. To resolve these contributions quantitatively, and assess potential secondary effects, such as CL at elevated voltages, we now analyze the float current behavior in combination with the scaling factor model. The capacity loss rate is used to correlate with the measured float current at 30 °C, as described in the following section.

3.2. Float Current and Scaling Factor Analysis

In this section, the analysis of the measured float currents across temperatures ranging from 5 °C to 50 °C, alongside the determination and evaluation of the scaling factors for both cells, will be presented.

3.2.1. Scaling Factor Determination Based on GITT Measurements

The scaling factor is determined from the OCV curves recorded during charge and discharge using GITT.^[42] This method incrementally adjusts the SoC with extended relaxation periods, minimizing kinetic effects and enabling a more accurate determination of equilibrium potentials compared to quasiOCV approaches.^[43] The protocol includes 74 SoC steps with 1 h rest periods, applying 0.1 C currents for both charge and discharge.

As both cells use graphite anodes, the average of the charge and discharge curves is used to generate the DVA. Although the LFP cathode exhibits significant hysteresis, this primarily affects the absolute voltage and only at very low voltages the shape or slope of the curve with negligible impact on the scaling factor that is close to 1. Since our method relies on the relative slopes to determine the scaling factors, and the voltage offset introduced by the hysteresis is small in comparison, the influence on the analysis is minimal and effectively accounted for. From the full

cell DVA, electrode-specific contributions are estimated using an educated guess based on known peak features and validated by the LLI-induced shift pattern described in prior work.^[16,44] This electrode separation is illustrated for the PAN cell in Figure 8a and for the A123 cell in Figure 8d. The reconstructed half-cell OCV curves for both cells are shown in Figure 8b for the PAN and Figure 8e for the A123, and exhibit typical characteristics for the corresponding electrode materials. Based on these curves, we calculate the individual scaling factor for both electrodes for each cell according to Equation (1) for the anode and (Equation 2) for the cathode, shown in Figure 8f for the A123 and Figure 8c for the PAN. The x-axis in these figures reflects capacity, but in the following analysis, the results are referenced against voltage. This transformation affects the shape of the scaling factor, particularly in the case of A123, whose voltage curve remains flat over most of the SoC range and only increases sharply at high SoC, unlike the PAN cell.

To examine the impact of aging on the scaling factor, we performed GITT measurements at 30 °C for two A123 cells: one fresh and one aged (3.6 V float aged), using the same protocol.

The anode scaling factors SF_A are shown in Figure 9a for the fresh cell and in Figure 9b for the aged cell at 3.6 V. While the general shape of the scaling factor remains unchanged, the curves shift toward higher voltages during aging. This behavior reflects the leftward shift of the cathode OCV curve, while the anode remains fixed. Since the cathode governs the full cell potential, this relative shift causes the same float voltage to correspond to different electrode lithiation states over time.

The voltage shift is most pronounced in the mid-voltage range (3.25–3.4 V), where the change in the scaling factor is most significant. Although float voltages remain fixed, the evolving lithiation ratio between anode and cathode alters the slope ratio of their respective OCV curves, reflected in the scaling factor SF .

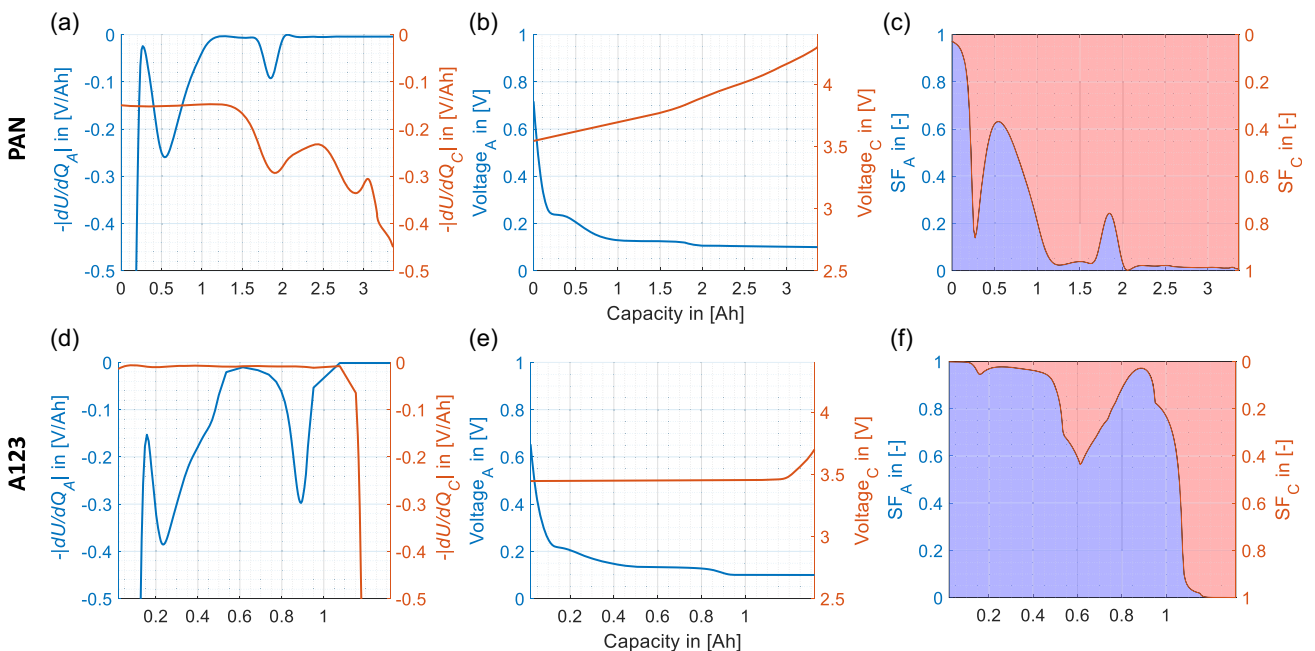


Figure 8. PAN a) half-cell DVA based on the educated guess resulting from the GITT measurement, b) the resulting half-cell OCV curve as validation, and c) the scaling factor for both electrodes. A123 d) half-cell DVA based on the educated guess resulting from the GITT measurement, e) the resulting half-cell OCV curve as validation, and f) the scaling factor for both electrodes. The anode curves are in the blue shade and the cathode curves are in the red shade.

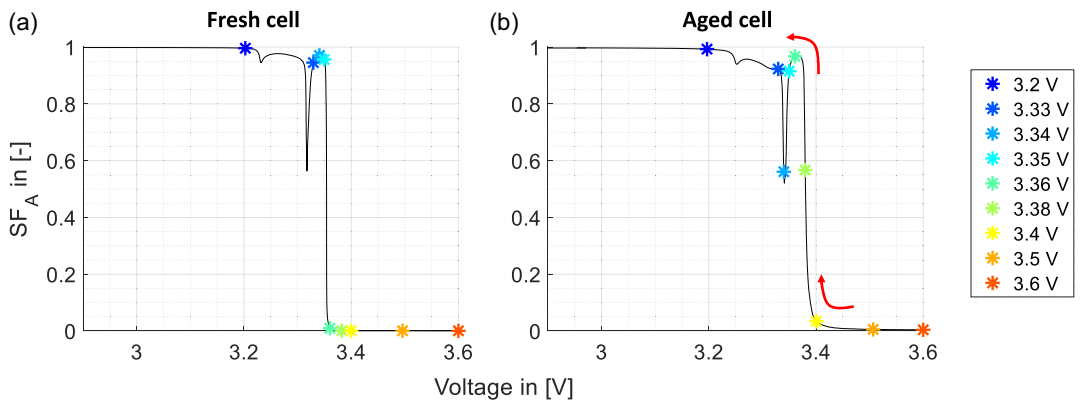


Figure 9. Measured SF_A of the A123 for a) a fresh cell and b) an aged cell with each float voltage having a distinctive color.

These changes have direct implications for our float current analysis: because the scaling factor defines how I_{float} is decomposed into I_{SEI} and I_{CL} , aging-induced shifts must be considered to avoid misinterpretation. In particular, at lower voltages where the deviation becomes large, using an outdated scaling factor leads to systematic errors in estimating electrode-specific degradation currents.

3.2.2. Measured Float Current over Temperature Steps

The float currents for several voltages over several temperature steps and its corresponding scaling factor SF_A for the PAN cell are shown in Figure 10a,c, respectively. For the A123 cell, these are presented in Figure 10b,d.

For each float voltage, the measured float current I_{float} increases consistently with rising temperature, as expected from thermally activated degradation processes. However, the float current does not increase monotonically with voltage. At certain voltages, such as between 3.75 and 3.821 V for the PAN cell, a higher float voltage corresponds to a lower float current. This nonmonotonic trend is also observed in the A123 cell, particularly above 3.38 V.

To understand these trends, we compare the measured float currents to the previously determined electrode-specific scaling factors. The scaling factor, derived from the GITT-based OCV curves of fresh cells, exhibits a voltage-dependent shape that directly affects the observable float current. Notably, both cells display a maximum in the anode scaling factor in the mid-voltage

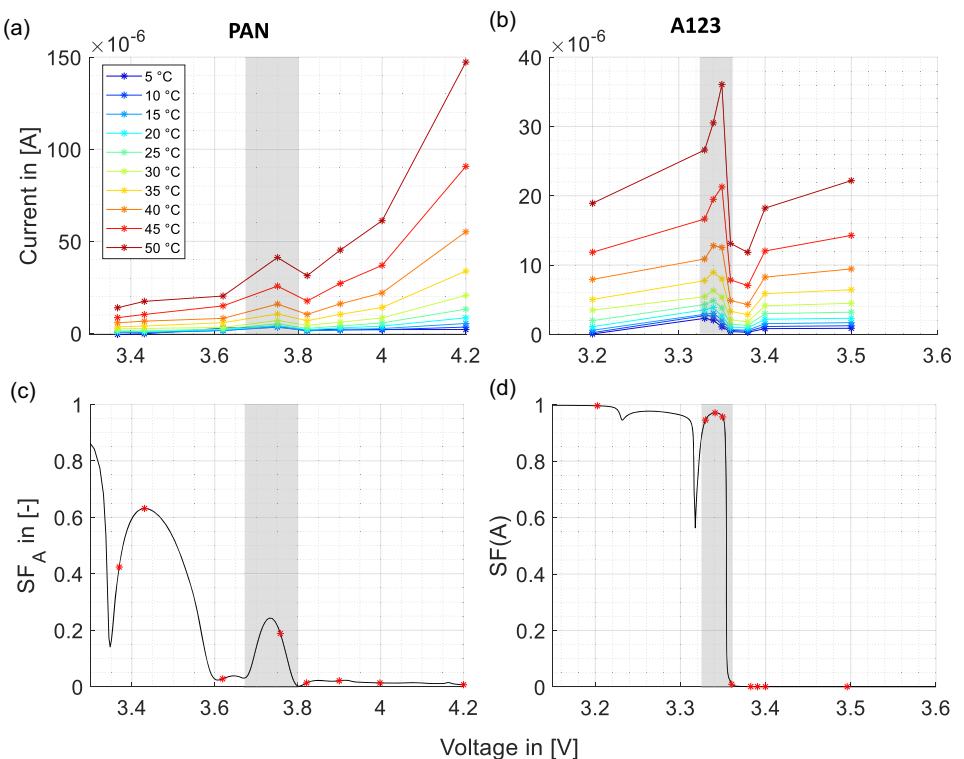


Figure 10. Measured I_{float} over temperature steps for the a) PAN and b) A123. The SF_A of the c) PAN and d) A123. The measured corresponding float voltages are labeled in red.

range, followed by a steep drop at higher voltages. This matches the voltage region where float current anomalies appear.

For example, in the PAN cell, the float current at 3.75 V is higher than at 3.821 V, despite the latter being a higher voltage. This reflects the steep decrease in the anode scaling factor, which modulates the contribution of electrode-specific degradation processes to the total recharge current. A similar trend is observed in the A123 cell, where float currents remain significant above 3.38 V despite a near-zero anode scaling factor.

These findings confirm that float current is not a direct proxy for degradation rate, but a voltage-dependent, scaled representation shaped by the anode scaling factor. When SF_A declines at elevated voltages, ongoing degradation is less strongly expressed in the observable float current I_{float} . This resolves the apparent discrepancy where higher float voltages result in lower measured current.

While the absolute float current may include contributions from both anode- and cathode-side processes, the scaling factor determines how these contributions appear at the cell level. A more detailed analysis of this decomposition, specifically the derivation of $I_{\text{SEIgrowth}}$ and I_{CL} , is presented in the next section.

3.3. Determination of the SEI Growth and CL Current

In the next step, the measured data comprising I_{loss} , I_{float} , SF_C , and SF_A are used as inputs for the self-developed model to calculate the electrode-specific degradation currents $I_{\text{SEIgrowth}}$ and I_{CL} . As the check-up procedure was conducted at 30 °C,

only the corresponding float current data at 30 °C is considered. The model is implemented in MATLAB 2023 and is based on the numerical solution of (Equations 3) and (4), representing the capacity and float domains. The goal is to optimize $I_{\text{SEIgrowth}}$ and I_{CL} such that the calculated values of I_{loss} and I_{float} match the measured data. Initial estimates are obtained by direct calculation from the equations, and serve as starting values for the optimization.

A challenge arises in the decomposition of I_{loss} and I_{float} into $I_{\text{SEIgrowth}}$ and I_{CL} when the scaling factor does not clearly favor one electrode, leading to multiple mathematically valid but potentially unphysical solutions. To constrain the solution space and ensure physical consistency, we apply three assumptions. First, we assume that CL is a secondary mechanism, such that $I_{\text{CL}} < I_{\text{SEIgrowth}}$. Second, both degradation currents are assumed to increase monotonically with float voltage, reflecting their electrochemical activation behavior, in agreement with literature for the relevant voltage range.^[45,46] Third, we consider I_{loss} and I_{float} as fixed inputs, assuming that reversible effects, such as the anode overhang, have sufficiently decayed at the time of measurement. Under these conditions, the scaling factor is treated as the only variable parameter during optimization. These assumptions enable the identification of a unique and physically meaningful solution from the set of mathematically valid possibilities. As discussed in Section 3.2, the scaling factor is affected by the aging-induced voltage slippery. In Figure 9, an approximate

shift of 0.03 V is observed between the aged and fresh cells, which is used to set the bounds for the scaling factor. Depending on the respective float voltage, the respective change in scaling factor for the 0.03 V range can be small or high and will be indicated with an errorbar. As we consider solely LLI, this shift only occurs towards smaller voltages due to LLI, as shown in Figure 9.

To efficiently and effectively find the global minimum or maximum of a function with continuous variables, the **GlobalSearch** procedure of the MATLAB Optimization Toolbox is used.^[47] To avoid local minima and maxima, **fmincon**^[48] is employed to explore a wider range of starting points and minimize the errors between the measured and simulated values.

Figure 11a shows the calculated $I_{\text{SEI growth}}$ and I_{CL} for the PAN cell, along with the measured (orange) and modeled (green) $I_{\text{C loss}}$. It is evident that there is a strong agreement between the measurements and the model. The error bars on $I_{\text{SEI growth}}$ and I_{CL} indicate the degree of freedom in scaling factor due to LLI. Notably, at higher voltages, the error bars are nearly invisible as the scaling factor is nearly constant over a wide range. Below 3.5 V, I_{CL} is nearly zero, but it starts to increase significantly at 4.0 V. The maximum value for I_{CL} is around 20 μA , while $I_{\text{SEI growth}}$ reaches a maximum of 57 μA , with a minimum of 19 μA .

Multiplying the data obtained from the check-up with the corresponding scaling factor results in the simulated I_{float} , which is plotted in Figure 11c. The only major discrepancy occurs at 3.432 V, which is at a relatively low SoC where the scaling factor is more challenging to determine compared to higher SoCs. We also observe that $I_{\text{SEI growth}}$ is the only aging mechanism at lower SoCs, while I_{CL} contributes at higher SoCs in the float domain along the $I_{\text{SEI growth}}$. This contribution of CL at higher voltages for nickel-cobalt-aluminum-based cells was also observed by Keil et al.^[29] In the middle voltage ranges, a mixture of both effects is evident.

For the A123 an increasing $I_{\text{SEI growth}}$ is observed across the entire voltage range, while I_{CL} remains almost constant at 1.2 μA , only beginning to rise at 3.38 V and continuing to increase until it reaches a maximum of 5 μA (see Figure 12a). Once again, the model and measurements show a strong agreement for measured and modeled $I_{\text{C loss}}$, similar to the results for the PAN cell. Interestingly, at 3.4 V, $I_{\text{C loss}}$ is higher than at 3.5 V, despite the resistance at 3.4 V rising by only 6%, compared to an 11% increase at 3.5 V (see Figure 5b). This discrepancy aligns with the CL theory, where lithiation temporarily masks capacity loss while contributing to a rise in cell resistance. When examining the simulated I_{float} and comparing it with the measurements,

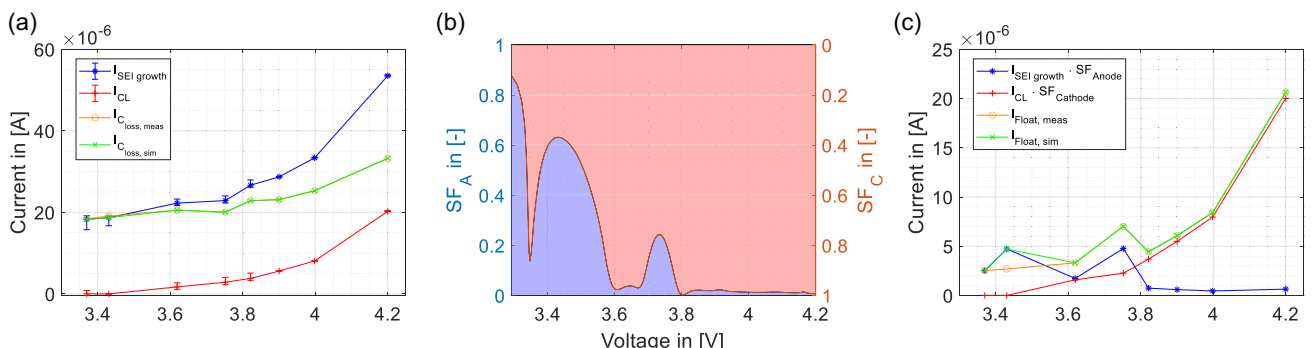


Figure 11. PAN a) modeled $I_{\text{SEI growth}}$ in blue as well as I_{CL} in red with errorbars indicating the possible range of each current, and the measured $I_{\text{C loss}}$ in orange and modeled $I_{\text{C loss}}$ in green. b) The scaling factor for both electrodes of the PAN cell and c) the resulting I_{float} from the model in green compared to the measurement in orange. The currents are plotted versus the voltage.

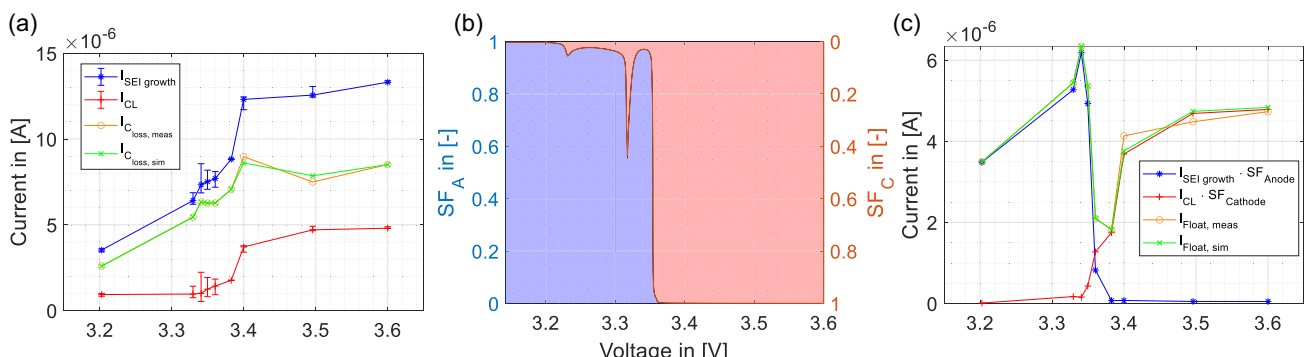


Figure 12. A123 a) modeled $I_{\text{SEI growth}}$ in blue as well as I_{CL} in red with errorbars indicating the possible range of each current, and the measured $I_{\text{C loss}}$ in orange and modeled $I_{\text{C loss}}$ in green. b) The scaling factor for both electrodes of the A123 cell and c) the resulting I_{float} from the model in green compared to the measurement in orange. The currents are plotted versus the voltage.

a relatively high agreement is observed, with a clear contribution from each electrode being identifiable. At lower voltages, the anode is nearly the only contributor, while at higher voltages, the increasing influence of the cathode becomes evident. Looking at the A123 cell from the SoC perspective, as depicted in **Figure A1a**, we observe that the CL effect starts to contribute significantly at an SoC of around 87%. This finding is consistent with the studies by Rumberg et al.^[49] where the loss of SoH peaked at around 80–90% SoC. This further validates the increase of the CL effect occurring at higher voltage ranges.

Overall, the model and theories demonstrated strong agreement between the measured and modeled data, highlighting the impact of electrolyte decomposition leading to CL. In the following section, we aim to extend the knowledge for I_{loss} , $I_{\text{SEIgrowth}}$, and I_{CL} gained from the reference temperature of 30 °C to the temperature range measuring only I_{float} during temperature steps.

3.4. Model Extension for the Determination of the SEI Growth and CL Current Using Float Current Temperature Steps

The temperature profiles are only measured for the I_{float} . As a first step, we take a closer look at the measured temperature steps for both cells from a different perspective, as shown in **Figure 13a** for the PAN cell and **Figure 13b** for the A123 cell.

We observe that the float current I_{float} for both cells follows the Arrhenius law.^[6,20,50] However, the sequence of I_{float} does not always align with the sequence of cell potentials, particularly for the A123. This phenomenon confirms the voltage slippery theory as explained by Azzam et al.^[34] as at lower cell voltages, anode effects are dominant and at higher cell voltages cathode effects become more dominant, as confirmed by Azzam et al.^[33] Based on the Arrhenius behavior of I_{float} , we assume that both $I_{\text{SEIgrowth}}$ and I_{CL} also adhere to the Arrhenius law,^[51] as demonstrated by Alipour et al.^[52] where SEI formation, solid-state electrolytes, and ionic liquids all followed this behavior. Particularly, the electrolyte, whose decomposition could lead to CL, further supports this assumption.^[30]

We begin with the equation used to fit our measured float current I_{float}

$$I_{\text{float,Model}} = a \cdot \exp^{(-b \cdot T)} \quad (5)$$

in Equation (5), a is a shape factor and b reflects the rate of change with temperature. After extracting the $I_{\text{SEIgrowth}}$ and I_{CL} for the 30 °C, the currents treated as fixed values in the optimization and serve as true points for fitting for the estimation the $I_{\text{SEIgrowth}}$ and I_{CL} for other temperature steps based on the fit of the float current $I_{\text{float,Model}}$.

We also assume that the same ratio between $I_{\text{SEIgrowth}}$ and I_{CL} applies across all temperature steps, implying that both effects behave similarly regarding the Arrhenius law. Additionally, $I_{\text{SEIgrowth}}$ and I_{CL} are expected to increase with increasing voltages and increasing temperatures.

Another factor to consider is the temperature sensitivity of the scaling factor. As shown by Streck et al.^[26] electrode behavior changes with temperature, affecting the slope of the voltage curves and thus the scaling factor. This trend is indirectly supported by our float current data. For the A123 cell, shown in **Figure A3**, the float current at 3.33 V is highest at low temperatures but becomes the lowest at higher temperatures, with 3.35 V showing the opposite trend. These shifts suggest a temperature-dependent change in the effective position on the scaling factor curve. Although we do not directly measure temperature-resolved scaling factors, both the observed float current behavior and the DVA sensitivity support the assumption of temperature dependence. We therefore allow for a temperature-dependent adjustment of the effective scaling factor bounds, while keeping the overall shape fixed to the 30 °C baseline. While this approach is supported indirectly by observed float current behavior and DVA sensitivity, we acknowledge that direct measurement of temperature-dependent scaling factors was not performed. Future work including temperature-resolved GITT experiments would be valuable to empirically validate and refine this aspect of the model.

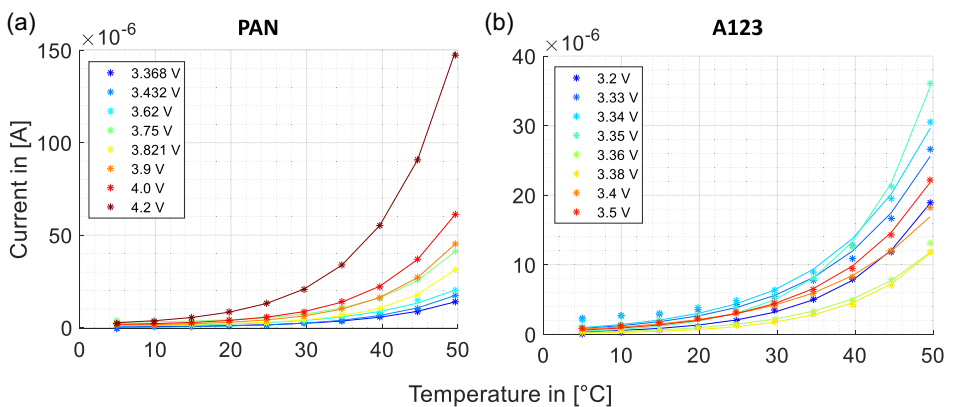


Figure 13. Measured float current I_{float} for the a) PAN and b) A123 for all cell voltages for the steps profile (stars) and a simple exponential fit for the measured aging current (line).

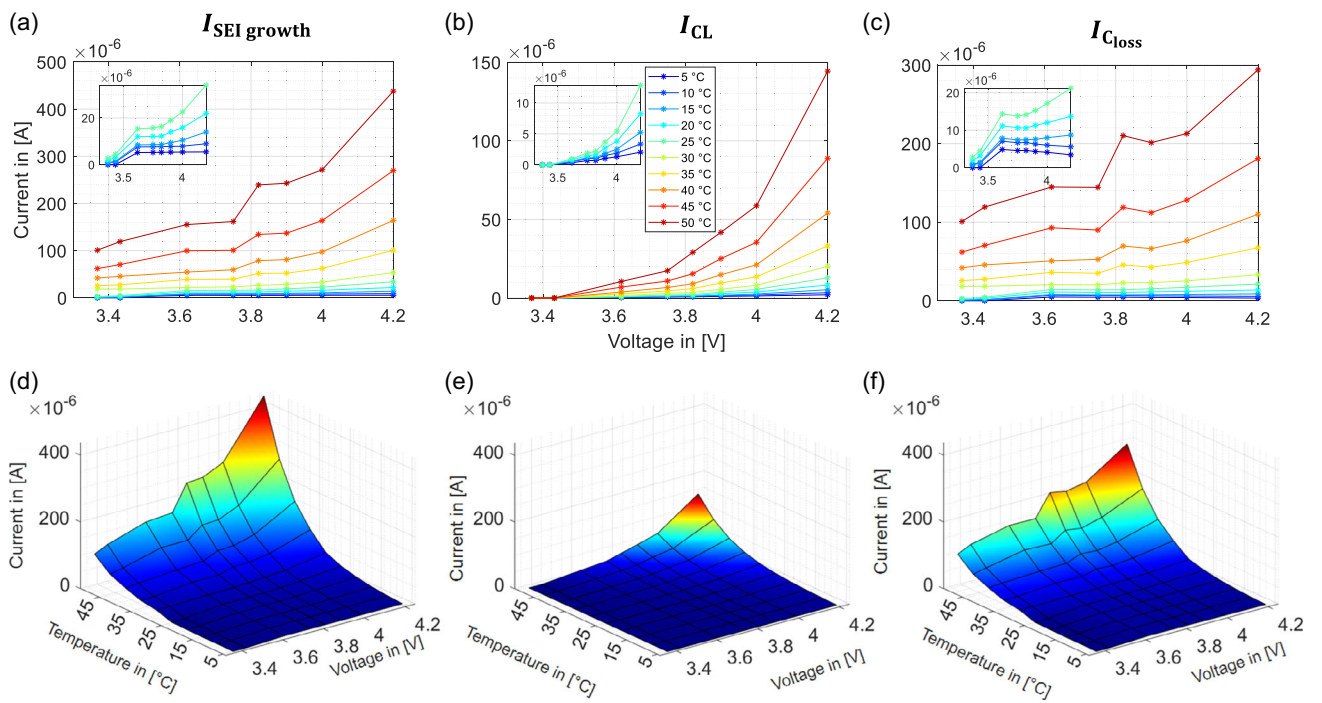


Figure 14. Calculated currents of the PAN cell for the a) $I_{SEI\text{growth}}$, b) I_{CL} , and c) $I_{C\text{loss}}$ as a function of voltage across different temperatures with zoomed in sections for the temperature range between 5–25 °C, and its corresponding 3D plot for the d) $I_{SEI\text{growth}}$, e) I_{CL} , and f) $I_{C\text{loss}}$.

We then fit all our measured data simultaneously using the `fmincon` function with the **GlobalSearch** procedure from the MATLAB Optimization Toolbox.

The $I_{SEI\text{growth}}$ and I_{CL} of the PAN cell are depicted in Figure 14a, b. It becomes evident that both increasing temperature and increasing voltage result in higher currents. We observe that the maximum current for I_{CL} is 150 μ A at 4.2 V and 50 °C, while the maximum for I_{SEI} is 420 μ A, almost three times as much. This validates the theory that SEI formation, being the main mechanism of calendar aging, is dominant, while CL starts to take precedence at higher voltages.

When examining the resulting I_{float} from the optimization and comparing it to the measured I_{float} in Figure A2, we observe a high level of agreement. For the quantification of $I_{C\text{loss}}$, we subtract $I_{SEI\text{growth}}$ and I_{CL} according to (Equation 4), resulting in the values shown in Figure 14c. Notably, at 3.821 V and 50 °C, the capacity loss rate is higher than at 3.9 and 4.0 V. This suggests that storing the PAN cell at this lower voltage could lead to a higher capacity loss rate. However, this does not imply that the cell's lifespan regarding cycling would necessarily be longer at 3.9 or 4.0 V compared to 3.821 V. Hartmann et al.^[30] reported that cells stored at 100% SoC exhibited lower capacity losses than those at 80% SoC, but when cycling began, the cells at 100% SoC failed after 20 cycles, unlike those at 80% SoC. This same phenomenon, attributed to electrolyte decomposition, was also confirmed in their study.

A closer examination of the 3D plots in Figure 14d,e, for $I_{SEI\text{growth}}$ and I_{CL} , respectively, reveals an exponential increase in the calculated currents, further supporting the Arrhenius law assumption for both effects. Additionally, the effect of CL peaks at the highest voltage and temperature, while SEI formation is

consistently present, even at lower SoCs and temperatures. Another representation that further validates this behavior can be found in the Appendix, where $I_{C\text{loss}}$, $I_{SEI\text{growth}}$, and I_{CL} follow the Arrhenius law (see Figure A4a,c).

Moreover, further studies have demonstrated that calendar aging, quantified through the capacity loss rate, also adheres to the Arrhenius behavior.^[50,53–55] This is a logical conclusion, as both SEI growth and CL, the primary contributors to capacity loss, are governed by temperature-dependent kinetics. Consequently, the overall capacity loss rate exhibits an Arrhenius-based exponential increase with temperature, further validating our model.

The same optimization and calculation procedure is applied to the A123 cell. As mentioned earlier, the A123 cell at 3.6 V did not undergo the temperature profile. In Figure 15a,b the $I_{SEI\text{growth}}$ and I_{CL} are shown. Similar to the PAN cell, the currents for the A123 cell increase with both temperature and voltage. Additionally, the measured and calculated I_{float} show a high level of agreement, as seen in Figure A3. An interesting phenomenon is observed when calculating the capacity loss rate. The maximum capacity loss rate is at 3.38 V, reaching $\approx 52 \mu$ A at 50 °C. Comparing this to the higher voltages at 3.4 and 3.5 V, it becomes clear that the CL effect is much stronger at these two voltage points. This is evident in Figure 15b for CL, where a noticeable increase is observed, in contrast to the SEI, which shows only a marginal increase. The exponential increase in $I_{SEI\text{growth}}$, I_{CL} , and $I_{C\text{loss}}$ is also clearly depicted in Figure 15d-f and also in Figure A5a–c.

We conclude that even in cell types with different cathode materials, the effect of CL is undeniable. This finding

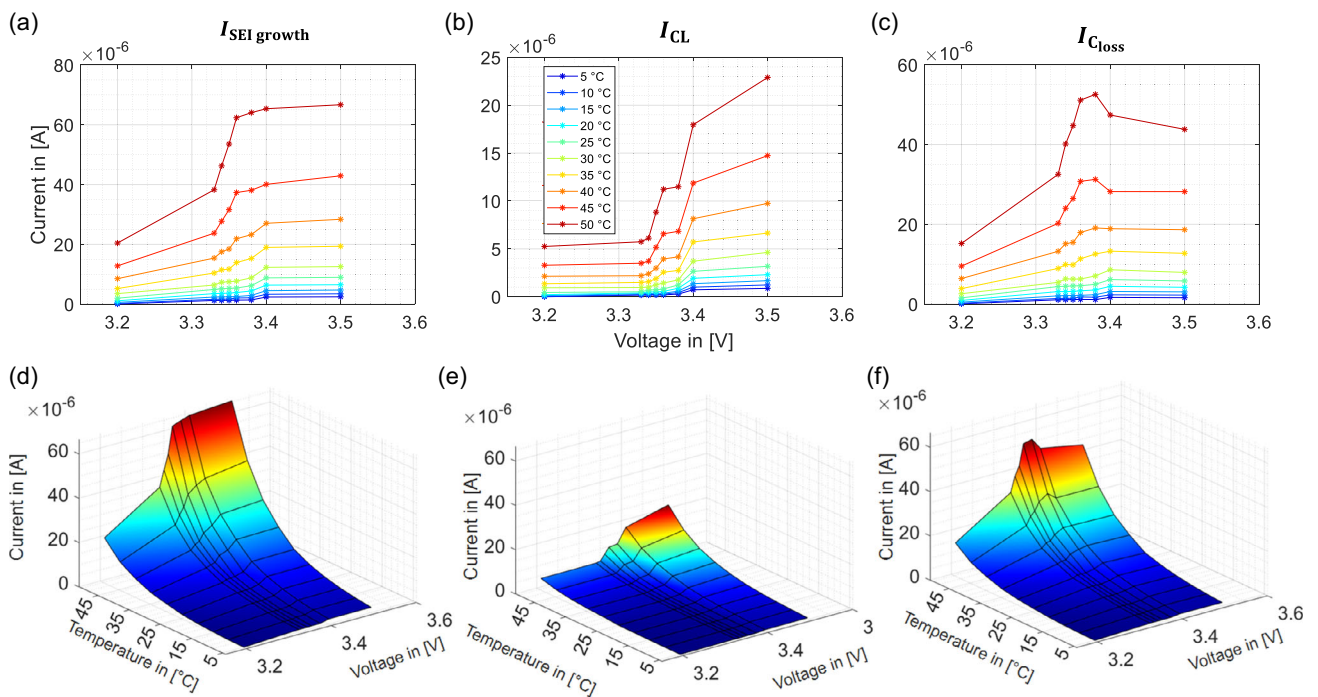


Figure 15. Calculated currents of the A123 cell for the a) $I_{\text{SEI growth}}$, b) I_{CL} , and c) I_{Closs} as a function of voltage across different temperatures and its corresponding 3D plot for the d) $I_{\text{SEI growth}}$, e) I_{CL} , and f) I_{Closs} .

demonstrates that, alongside the primary aging mechanism of SEI formation, CL must also be considered when quantifying calendar aging mechanisms. Additionally, the negligible contribution of the shuttle reaction further validates our assumptions, as the observed increase in internal resistance aligns more closely with CL mechanisms. By combining float current measurements with the classical check-up method, both aging mechanisms can be effectively quantified, leading to a more comprehensive understanding of cell aging.

4. Conclusions

This study investigated the calendar aging mechanisms of two types of lithium-ion cells using both conventional capacity tests and float current analysis. Initially, aging mechanisms were identified through standard capacity, resistance, and DVA tests, revealing a linear capacity loss rate primarily due to LLI, once the anode overhang effect was concluded.

The research provided a thorough analysis of float current behavior, emphasizing the interplay between SEI formation, and CL as key contributors to LLI during calendar aging. By examining different cell types with varying cathode materials, the study demonstrated that CL plays a crucial role at higher voltages, complementing the well-documented influence of SEI growth.

A central element of our analysis is a model that links measured float currents to electrode-specific degradation currents and capacity loss. This model uses voltage-dependent scaling factors, which reflect the differing voltage responses of the anode

and cathode. These factors change with SoC and aging, and are essential to accurately separate float current contributions.

By combining scaling factors with float current measurements and capacity loss rates from check-up tests, we quantify the degradation currents attributed to SEI growth and CL. Each contributes to the float current in proportion to its respective scaling factor. At 30 °C, the model yields consistent results across all tested voltages, validating the decomposition. No evidence of shuttle reactions was observed, supporting the interpretation that SEI growth and CL are the dominant degradation mechanisms under the investigated conditions.

The model was further extended to quantify degradation currents across a temperature range of 5–50 °C, using only float current data. Without requiring additional check-up measurements, the temperature dependence is described using the Arrhenius law, with activation energies fitted from 30 °C data. The scaling factors, assumed to change with temperature, allow SEI and CL contributions to be tracked under varying thermal conditions, providing a practical tool for aging assessment in real-world scenarios. However, since scaling factors were not directly measured at different temperatures, this assumption introduces a model limitation that should be addressed in future studies.

This dual consideration of SEI growth and CL, coupled with accurate scaling factor adjustments, can enhance battery management strategies and lead to the development of batteries with longer lifespans and improved performance stability. Future research should explore applying this methodology to cells with silicon-graphite anodes and comparing their behavior to similar cells. Additionally, integrating EIS measurements would provide further resistive data to verify the proposed theory.

Appendix

Figure A1 illustrates the modeled degradation currents $I_{SEI\text{growth}}$ and I_{CL} , scaling factors SF, float current I_{Float} , and capacity loss rate $I_{C_{\text{loss}}}$ for the A123 cell plotted against SoC, providing a reference for interpreting voltage-based trends in the main text.

Figure A2 compares the measured and simulated float currents across the full temperature range for the PAN cell. The simulation closely follows the experimental data at most temperatures and voltages, particularly above 15 °C, validating the model's accuracy. Minor deviations at lower temperatures may arise from increased noise and reduced current resolution, but the overall voltage trend and temperature dependence are well captured.

Figure A3 compares the measured and simulated float currents across the full temperature range for the A123 cell. The simulation closely follows the experimental data at most temperatures and voltages, particularly above 10 °C, validating the model's accuracy. Minor deviations at lower temperatures may arise from increased noise and reduced current resolution, but the overall voltage trend and temperature dependence are well captured.

Figure A4 illustrates the temperature dependence of the calculated aging currents for the PAN cell. All currents exhibit an exponential increase with temperature, consistent with Arrhenius behavior. Across all voltages, $I_{SEI\text{growth}}$ remains higher than I_{CL} , reinforcing its dominant role in lithium loss. The voltage-dependent increase is most pronounced for I_{CL} , especially at higher temperatures and float voltages, reflecting the growing influence of CL under harsh conditions.

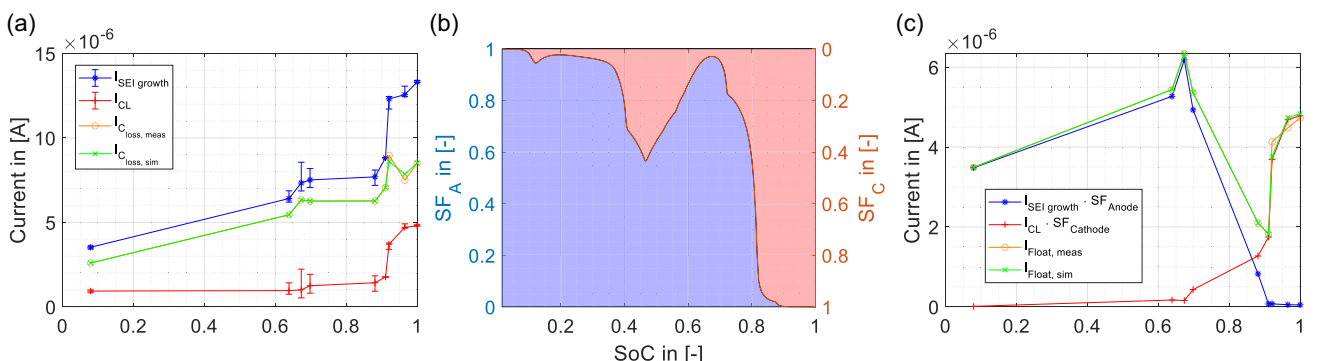


Figure A1. A123 a) modeled $I_{SEI\text{growth}}$ in blue as well as I_{CL} in red with errorbars indicating the possible range of each current, and the measured $I_{C_{\text{loss}}}$ in orange and modeled $I_{C_{\text{loss}}}$ in green. b) The scaling factor for both electrodes of the A123 cell and c) the resulting I_{float} from the model in green compared to the measurement in orange. The currents are plotted versus the SoC.

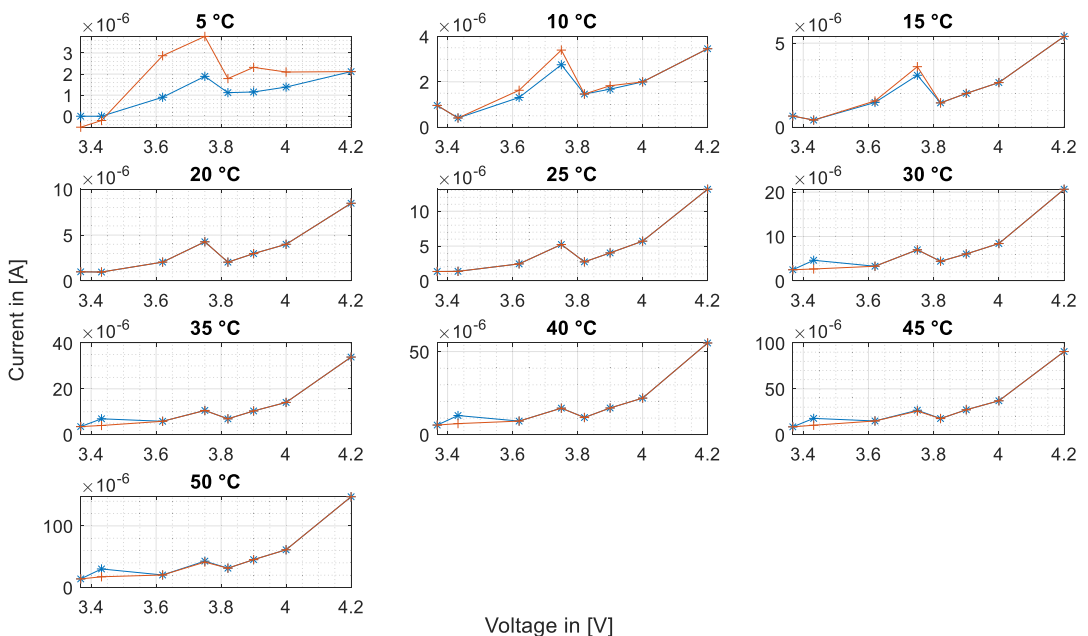


Figure A2. Measured (red) and simulated (blue) float currents I_{float} for the PAN cell for the temperature steps from 5 to 50 °C for all voltages.

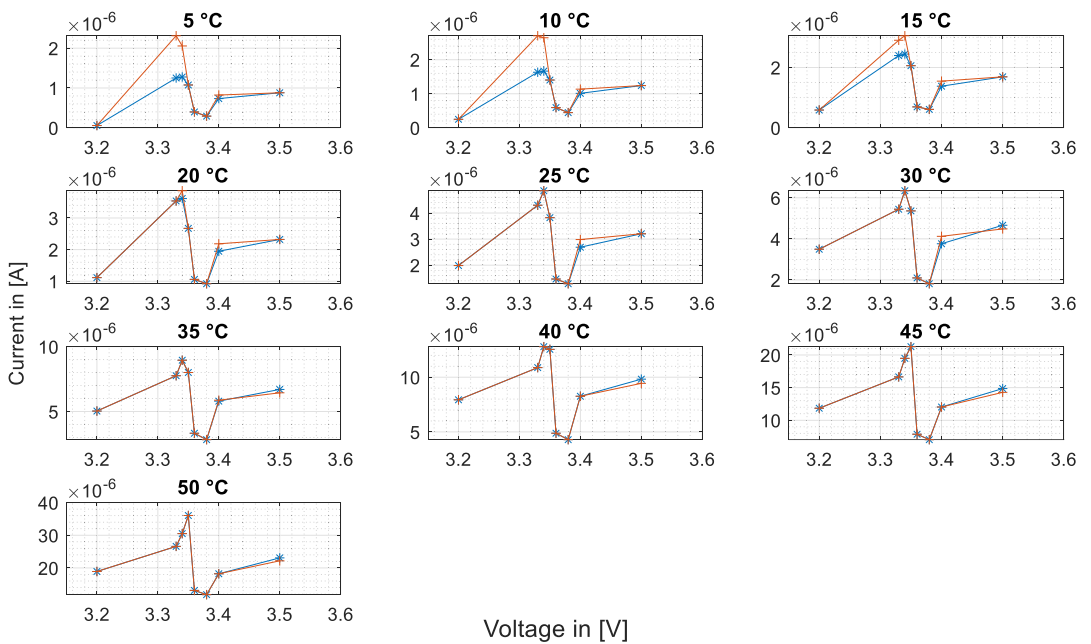


Figure A3. Measured (red) and simulated (blue) float currents I_{float} for the A123 cell for the temperature steps from 5 to 50 °C for all voltages except 3.6 V.

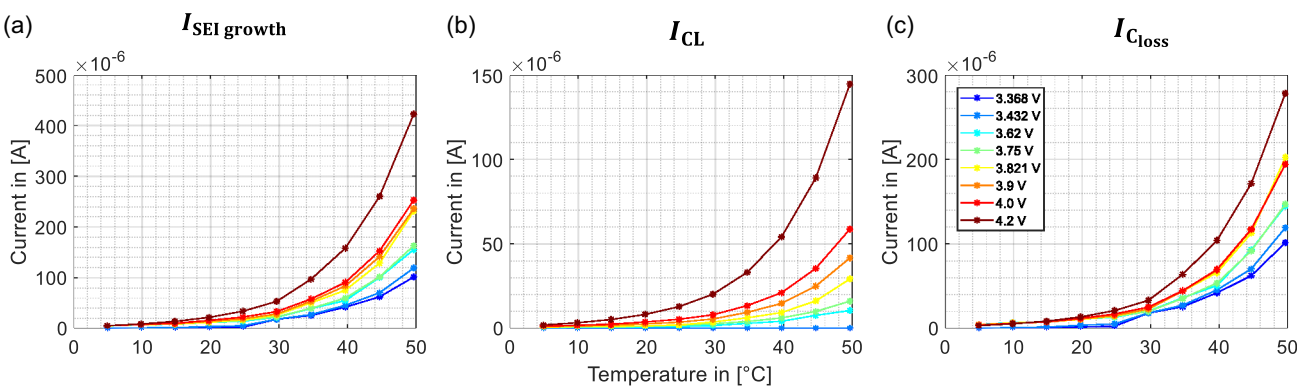


Figure A4. Calculated currents of the PAN cell for the a) $I_{\text{SEI growth}}$, b) I_{CL} , and c) I_{Closs} as a function of temperature across different voltages.

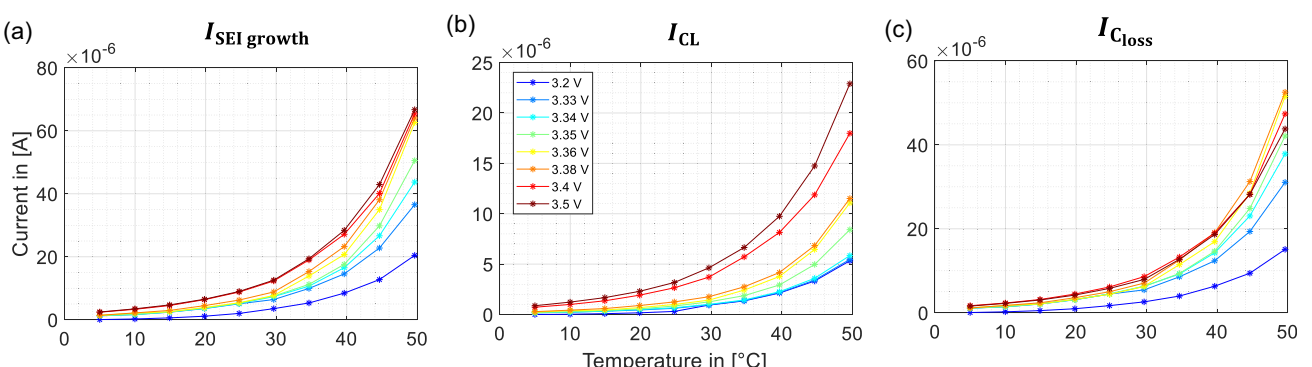


Figure A5. Calculated currents of the A123 cell for the a) $I_{\text{SEI growth}}$, b) I_{CL} , and c) I_{Closs} as a function of temperature across different voltages.

Figure A5 illustrates the temperature dependence of the calculated aging currents for the A123 cell. All currents exhibit an exponential increase with temperature, consistent with Arrhenius behavior. Across all voltages, I_{SEgrowth} remains higher than I_{CL} , reinforcing its dominant role in lithium loss. The voltage-dependent increase is most pronounced for I_{CL} , especially at higher temperatures and float voltages, reflecting the growing influence of CL under harsh conditions.

Acknowledgements

The research is funded by two projects. 1) Grant number: 440701024 funded by German Research Foundation (DFG); 2) Grant number: 03XP0442 funded by German Federal Ministry of Education and Research (BMBF). We acknowledge support by the Open Access Publication Fund of Technische Hochschule Ingolstadt (THI). Special thanks for the fruitful discussion and support to Qing Yu, Iqra Kiran, Andriy Taranovskyy, Moritz Ehrensberger, and Simon Diehl.

Conflict of Interest

The authors declare no conflict of interest.

Data Availability Statement

The data that support the findings of this study are available on request from the corresponding author. The data are not publicly available due to privacy or ethical restrictions.

Keywords: cathode lithiation · electrolyte decomposition · float current analysis · modelling · potentiostatic hold · self-discharge rate · solid electrolyte interphase

- [1] S. G. Marquis, PhD thesis, University of Oxford 2020.
- [2] A. Barré, B. Deguilhem, S. Grolleau, M. Gérard, F. Suard, D. Riu *J. Power Sources* **2013**, *241*, 680.
- [3] M. Kassem, C. Delacourt, *J. Power Sources* **2013**, *235*, 159.
- [4] C. R. Birk, M. R. Roberts, E. McTurk, P. G. Bruce, D. A. Howey, *J. Power Sources* **2017**, *341*, 373.
- [5] M. Naumann, M. Schimpe, P. Keil, H. C. Hesse, A. Jossen, *J. Energy Storage* **2018**, *17*, 153.
- [6] M. Ecker, J. B. Gerschler, J. Vogel, S. Käbitz, F. Hust, P. Dechent, D. U. Sauer, *J. Power Sources* **2012**, *215*, 248.
- [7] R. Mingant, J. Bernard, V. S. Moynot, A. Delaille, S. Mailley, J.-L. Hognon, F. Huet, *ECS Trans.* **2011**, *33*, 41.
- [8] M. Ecker, N. Nieto, S. Käbitz, J. Schmalstieg, H. Blanke, A. Warnecke, D. U. Sauer, *J. Power Sources* **2014**, *248*, 839.
- [9] S. Grolleau, I. Baghdadi, P. Gyan, M. Ben-Marzouk, F. Duclaud, *WEVJ* **2016**, *8*, 339.
- [10] M. Azzam, M. Ehrensberger, R. Scheuer, C. Endisch, M. Lewerenz, *Energies* **2023**, *16*, 3889.
- [11] M. Leverenz, J. Münnix, J. Schmalstieg, S. Käbitz, M. Knips, D. U. Sauer, *J. Power Sources* **2017**, *345*, 254.
- [12] M. Leverenz, G. Fuchs, L. Becker, D. U. Sauer, *J. Energy Storage* **2018**, *18*, 149.
- [13] T. Roth, L. Streck, A. Graule, P. Niehoff, A. Jossen, *J. Electrochem. Soc.* **2023**, *170*, 020502.
- [14] F. Hildenbrand, D. Ditscheid, E. Barbers, D. U. Sauer, *Appl. Energy* **2023**, *332*, 120395.
- [15] S. Käbitz, J. B. Gerschler, M. Ecker, Y. Yurdagel, B. Emmermacher, D. André, T. Mitsch, D. U. Sauer, *J. Power Sources* **2013**, *239*, 572.
- [16] P. Keil, S. F. Schuter, J. Wilhelm, J. Travi, A. Hauser, R. C. Katl, A. Jossen, *J. Electrochem. Soc.* **2016**, *163*, A1872.
- [17] D. Li, D. L. Danilov, L. Gao, Y. Yang, P. H. L. Notten, *J. Electrochem. Soc.* **2016**, *163*, A3016.
- [18] J. Belt, V. Utgikar, I. Bloom, *J. Power Sources* **2011**, *196*, 10213.
- [19] S. K. Rechkemmer, X. Zang, W. Zhang, O. Sawodny, *J. Energy Storage* **2020**, *30*, 101547.
- [20] J. de Hoog, J.-M. Timmermans, D. Ioan-Stroe, M. Swierczynski, J. Jaguemont, S. Goutam, N. Omar, J. van Mierlo, P. van den Bossche, *Appl. Energy* **2017**, *200*, 47.
- [21] B. Epding, B. Rumberg, H. Jahnke, I. Stradtmann, A. Kwade, *J. Energy Storage* **2019**, *22*, 249.
- [22] N. Bouchhima, M. Gossen, S. Schulte, K. P. Birke, *J. Energy Storage* **2018**, *15*, 400.
- [23] M. Lewerenz, S. Käbitz, M. Knips, J. Münnix, J. Schmalstieg, A. Warnecke, D. U. Sauer, *J. Power Sources* **2017**, *353*, 144.
- [24] M. Theiler, C. Endisch, M. Lewerenz, *Batteries* **2021**, *7*, 22.
- [25] M. C. Schulze, M.-T. F. Rodrigues, J. D. McBrayer, D. P. Abraham, C. A. Applett, I. Bloom, Z. Chen, A. M. Colclasure, A. R. Dunlop, C. Fang, K. L. Harrison, G. Liu, S. D. Minteer, N. R. Neale, D. Robertson, A. P. Tornheim, S. E. Trask, G. M. Veith, A. Verma, Z. Yang, C. Johnson, *J. Electrochem. Soc.* **2022**, *169*, 50531.
- [26] L. Streck, T. Roth, P. Keil, B. Strehle, S. Ludmann, A. Jossen, *J. Electrochem. Soc.* **2023**, *170*, 40520.
- [27] H. Qi, Y. Ren, S. Guo, Y. Wang, S. Li, Y. Hu, F. Yan, *ACS Appl. Mater. Interfaces* **2020**, *12*, 591.
- [28] G. R. Molaeimanesh, S. M. Mousavi-Khoshdel, A. B. Nemati, *J. Therm. Anal. Calorim.* **2021**, *143*, 3137.
- [29] P. Keil, A. Jossen, *J. Electrochem. Soc.* **2017**, *164*, A6066.
- [30] L. Hartmann, L. Reuter, L. Wallisch, A. Beiersdorfer, A. Adam, D. Goldbach, T. Teufel, P. Lamp, H. A. Gasteiger, J. Wandt, *J. Electrochem. Soc.* **2024**, *171*, 60506.
- [31] T. Boetticher, A. Adamson, S. Buechele, E. D. Alter, M. Metzger, *J. Electrochem. Soc.* **2023**, *170*, 60507.
- [32] M. Azzam, M. Ehrensberger, C. Endisch, D.-U. Sauer, M. Lewerenz, *Batteries Supercaps* **2025**, *8*, e202400627.
- [33] M. Azzam, M. Ehrensberger, C. Endisch, M. Lewerenz, *J. Energy Storage* **2024**, *102*, 114142.
- [34] M. Azzam, C. Endisch, M. Lewerenz, *Batteries* **2024**, *10*, 3.
- [35] B. Rumberg, B. Epding, I. Stradtmann, A. Kwade, *J. Energy Storage* **2019**, *25*, 100890.
- [36] R. Xiong, Y. Pan, W. Shen, H. Li, F. Sun, *Renewable Sustainable Energy Rev.* **2020**, *131*, 110048.
- [37] Q. Yu, I. Kiran, M. Ehrensberger, L. Streck, T. Roth, A. Jossen, C. Endisch, M. Lewerenz, *J. Electrochem. Soc.* **2025**, *172*, 060523.
- [38] X.-G. Yang, Y. Leng, G. Zhang, S. Ge, C.-Y. Wang, *J. Power Sources* **2017**, *360*, 28.
- [39] M. Leverenz, A. Marongiu, A. Warnecke, D. U. Sauer, *J. Power Sources* **2017**, *368*, 57.
- [40] T. Deutschen, S. Gasser, M. Schaller, J. Siehr, *J. Energy Storage* **2018**, *19*, 113.
- [41] W. Cao, J. Li, Z. Wu, *Ionics* **2016**, *22*, 1791.
- [42] W. Weppner, R. A. Huggins, *Annu. Rev. Mater. Sci.* **1978**, *8*.
- [43] V. Knap, D.-I. Stroe, *J. Power Sources* **2021**, *498*, 229913.
- [44] M. Simolka, J.-F. Heger, N. Traub, H. Kaess, K. A. Friedrich, *J. Electrochem. Soc.* **2020**, *167*, 110502.
- [45] A. Maheshwari, M. Heck, M. Santarelli, *Electrochim. Acta* **2018**, *273*, 335.
- [46] D. Li, D. Danilov, Z. Zhang, H. Chen, P. H. L. Notten, *J. Electrochem. Soc.* **2015**, *162*, A858.
- [47] Toolbox, Optimization, .Natick: The Mathworks Inc. MA, USA 2002.
- [48] Z. Ugray, L. Lasdon, J. Plummer, F. Glover, J. Kelly, R. Marti, *Informs J. Comput.* **2007**, *19*, 328.
- [49] B. Rumberg, B. Epding, I. Stradtmann, M. Schleder, A. Kwade, *J. Energy Storage* **2020**, *30*, 101510.
- [50] J. Schmalstieg, S. Käbitz, M. Ecker, D. U. Sauer, *J. Power Sources* **2014**, *257*, 325.

- [51] S. Ge, Y. Leng, T. Liu, R. S. Longchamps, X.-G. Yang, Y. Gao, D. Wang, D. Wang, C.-Y. Wang, *Sci. Adv.* **2020**, *6*, eaay7633.
- [52] M. Alipour, C. Ziebert, F. V. Conte, R. Kizilel, *Batteries* **2020**, *6*, 35.
- [53] M. Schimpe, M. E. von Kuepach, M. Naumann, H. C. Hesse, K. Smith, A. Jossen, *J. Electrochem. Soc.* **2018**, *165*, A181.
- [54] E. Sarasketa-Zabala, I. Gandiaga, L. M. Rodriguez-Martinez, I. Villarreal, *J. Power Sources* **2014**, *272*, 45.
- [55] E. Sarasketa-Zabala, E. Martinez-Laserna, M. Berecibar, I. Gandiaga, L. M. Rodriguez-Martinez, I. Villarreal, *Appl. Energy* **2016**, *162*, 839.

Manuscript received: May 7, 2025

Revised manuscript received: July 14, 2025

Version of record online:
